

The First Hillslope Thermokarst Inventory for the Permafrost Region of the Qilian Mountains

Xiaoqing Peng^{1,3}, Guangshang Yang¹, Oliver W. Frauenfeld², Xuanjia Li¹, Weiwei Tian¹, Guanqun Chen¹, Yuan Huang¹, Gang Wei¹, Jing Luo⁴, Cuicui Mu^{1,3}, Fujun Niu⁴

¹Key Laboratory of Western China's Environmental Systems (Ministry of Education), College of Earth and Environmental Sciences, Lanzhou University, Lanzhou, 730000, China

²Department of Geography, Texas A&M University, College Station, TX 77843-3147, USA

³Observation and Research Station on Eco-Environment of Frozen Ground in the Qilian Mountains, Lanzhou University, Lanzhou 730000, China

⁴State Key Laboratory of Frozen Soil Engineering, Northwest Institute of Eco-Environment and Resources, Chinese Academy of Sciences, Lanzhou 730000, China

* Corresponding author: Guangshang Yang (220220948511@lzu.edu.cn)

Abstract:

Climate warming and anthropogenic disturbances result in permafrost degradation in cold regions, including in the Qilian Mountains. These changes lead to extensive hillslope thermokarst (HT) formation, such as retrogressive thaw slumps, active-layer detachment slides, and thermal erosion gullies. These in turn cause, e.g., degradation of local vegetation, economic losses, infrastructure damages, and threats to human safety. However, despite its importance, there is currently no thermokarst inventory for the Qilian Mountains. Through manual visual interpretation and field validation, we therefore produce the first quantification of HT features. We count a total of 1064 HT features, with 67% located in the upper reaches of the Heihe River Basin, which encompasses ~13% of the Qilian Mountains region. We further identified that 187 HT features (18%) existed before 2010, while the remaining 874 (82%) were initiated in the recent period. More specifically, 392 sites (37%) were initiated during 2010–2015, and 482 (45%) after 2015. Thermokarst terrain is observed primarily in areas with shallow active layer depths (average thickness: 2.98 m) on northern shaded slopes of 3–25°, with low solar radiation and moderate elevations ranging from 3200 to 4000 m. This first inventory of HT features is an important and missing piece in documenting changes on the Qinghai-Tibetan Plateau, and this new dataset also provides an important basis for further studies, such as automated extraction of HT features, susceptibility analysis of HT, and estimating losses caused by HT. The datasets are available from the National Tibetan Plateau/Third Pole Environment Data Center and can be downloaded from <https://doi.org/10.11888/Cryos.tpd.300805> (Peng and Yang, 2023).

43 **1 Introduction**

44 The Qilian Mountains are located in the northeastern part of the Qinghai-Tibetan
45 Plateau, at the confluence of three major geographical regions that include the eastern
46 monsoon zone, the northwestern arid zone, and the alpine zone of the Qinghai-Tibetan
47 Plateau. The Qilian Mountains play an important role in maintaining the ecological
48 balance of the Tibetan Plateau, stopping the southward progression of deserts, and
49 maintaining the stability of the oases in the Hexi Corridor. Due to its unique
50 geographical and environmental characteristics, permafrost is widespread and
51 underlies about 50% of the area (Ran et al., 2021). Permafrost has an important role in
52 storing frozen water, thereby contributing to water conservation (Wang et al., 2022).
53 These roles can aid in inland river runoff recharge, which is crucial to regional
54 ecology, production, and life. Due to climate warming and human activities,
55 significant permafrost degradation results in the frequent occurrence of thermokarst,
56 representing a serious threat to ecological security and adversely impacts the
57 environment and human beings (Li et al., 2022a).

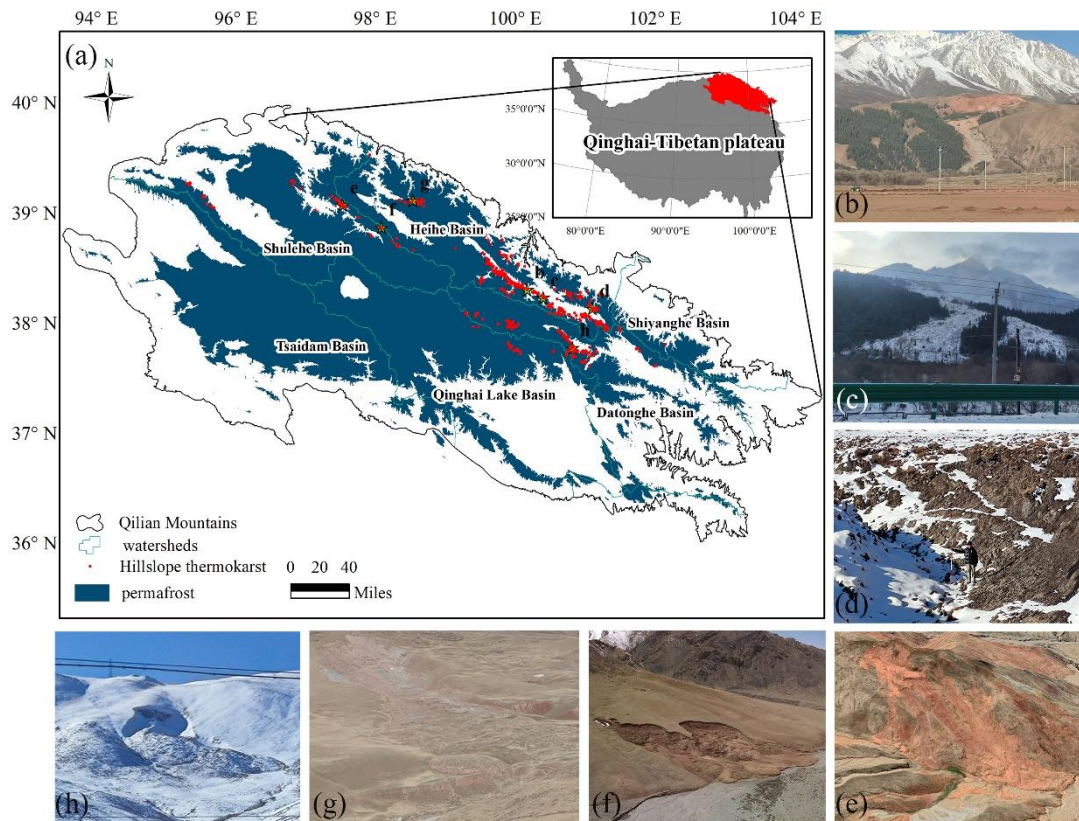
58 Despite the importance of thermokarst processes and their potential geohazards, the
59 distribution of thermokarst landscapes is currently mostly undocumented. The
60 available distribution of thermokarst in the Northern Hemisphere, including
61 retrogressive thaw slumps (RTSs), thermokarst lakes, and other terrain features,
62 represents mainly probabilistic estimates (Olefeldt et al., 2016; Yin et al., 2021;
63 Huang et al., 2023; Yang et al., 2023). Muster et al. (2017) determined the distribution
64 of circumpolar Arctic permafrost lakes and ponds from 2002–2013 at a resolution of 5
65 m using optical remote sensing, satellite (Geo-Eye, QuickBird, WorldView-1 and -2,
66 KOMPSAT-2), and radar imagery (TerraSAR-X), but temporal inconsistencies make
67 comparisons in time and space difficult. At the regional scale, the techniques and
68 spatial resolution of remote sensing imagery currently used at different study areas are
69 inconsistent, e.g., estimating the distribution and development of RTSs on Banks
70 Island, Canada, based on the interpretation of a Google Earth Engine Timelapse
71 dataset (Lewkowicz and Way, 2019). Satellite imagery at 30-m resolution from
72 Landsat has been used to analyze RTSs and thermokarst lakes in the region of Alaska
73 within the circumpolar Arctic, eastern Canada, and Siberia (Nitze et al., 2018). Nicu et
74 al. (2023) employed orthorectified imagery with a resolution of 5 meters to visually
75 interpret and identify cryospheric hazards (such as thaw slumps and thermo-erosion
76 gullies) in Nordenskiöld Land, covering an approximate area of 4000 square
77 kilometers in the Svalbard Archipelago. The permafrost zone of the Qinghai-Tibetan
78 Plateau (QTP) has been a site of thermokarst geomorphology research in recent years.
79 For example, combining field surveys and SPOT-5 satellite data for August 2010, a
80 total of 2,163 thermokarst lakes and ponds were recorded within 10 km on either side
81 of the Chumar River to Fenghuo Mountain of the Qinghai-Tibet Railway, with a total
82 surface area of $1.09 \times 10^7 \text{ m}^2$ and ranging in size from 100 m^2 to $4.49 \times 10^5 \text{ m}^2$ (Luo
83 et al., 2015; Niu et al., 2014). In the Beiluhe region of the central QTP, the number of
84 RTSs increased from 124 to 438 between 2008 and 2017, with an approximate 9-fold
85 increase in area (Huang et al., 2020; Luo et al., 2019). The latest results show that the
86 number of RTSs on the QTP is 2669, but for the Qilian Mountains in the northeastern
87 part of the region, only 6 (Luo et al., 2022) or as many as 15 are documented (Mu et
88 al., 2020). A lack of a thermokarst inventory in this region is therefore evident,
89 representing a crucial gap in the RTSs inventory on the QTP.

90 Frequent occurrence of hillslope thermokarst hazards due to permafrost degradation,

91 with significant ecological impacts on the Qilian Mountains. The ecological
92 environment of the permafrost areas has a significant impact, and there is a direct
93 correlation between human activities and major permafrost engineering problems,
94 including uneven subsidence of infrastructure, slumps, and cracks. Meanwhile, there
95 is little to no information regarding hillslope thermokarst (HT) features such as RTSs,
96 active-layer detachment slides, and thermo-erosion gullies (Gooseff et al., 2009) in
97 the Qilian Mountains. HT refers to a specific type of thermokarst formation that
98 occurs in permafrost regions. While it is similar to regular thermokarst, what
99 distinguishes hillslope thermokarst is its occurrence on sloped terrain or hillsides,
100 where permafrost thaw leads to slope instability. This can result in various landforms
101 like retrogressive thaw sumps, thermo-erosion gullies, or active layer detachments,
102 affecting the stability and shape of hillslopes in permafrost regions. These features can
103 significantly impact the landscape and have implications for infrastructure,
104 ecosystems, and land use in areas affected by hillslope thermokarst processes (Kokelj
105 and Jorgenson, 2013; Olefeldt et al., 2016; Gooseff et al., 2009). Thus, the urgent need
106 to survey and quantify these undocumented HT features in the Qilian Mountains
107 motivates and represents the goal of this study.

108 109 **2 Study Area**

110 The Qilian Mountains are located at the northern edge of the QTP, with an average
111 elevation of 3855 m. The region is underlain by permafrost and seasonally frozen
112 ground (36–40°N and 94–104°E, Figure 1a), with a permafrost area of 94,235 km²
113 that accounts for 49% of the study domain. Characterized by both an alpine mountain
114 climate and a temperate continental monsoon climate, the mean annual air
115 temperature is 0.30°C (Jin et al., 2022) with high precipitation variability and higher
116 amounts in the southeast during the thawing season of June to September (Chen et al.,
117 2013; Li et al., 2022b). Due to human activities, climate change, and earthquakes,
118 permafrost instability in Qilian Mountains has gradually increased, resulting in HT
119 formation including RTSs, active-layer detachment slides, and thermal erosion gullies,
120 which pose a direct threat to the local economy, ecology, and safety.



121

122 **Figure 1** The location of the study area and a) its HT distribution (Qilian Mountains
 123 permafrost extent data is from Sheng et al., 2020), and b)–h) HT features obtained
 124 from different watersheds during our field surveys with the exception of e) a Google
 125 Earth image, as this site is too difficult to access, the positions corresponding to b)–h)
 126 have been labeled in a).

127

128 3 Data Sources

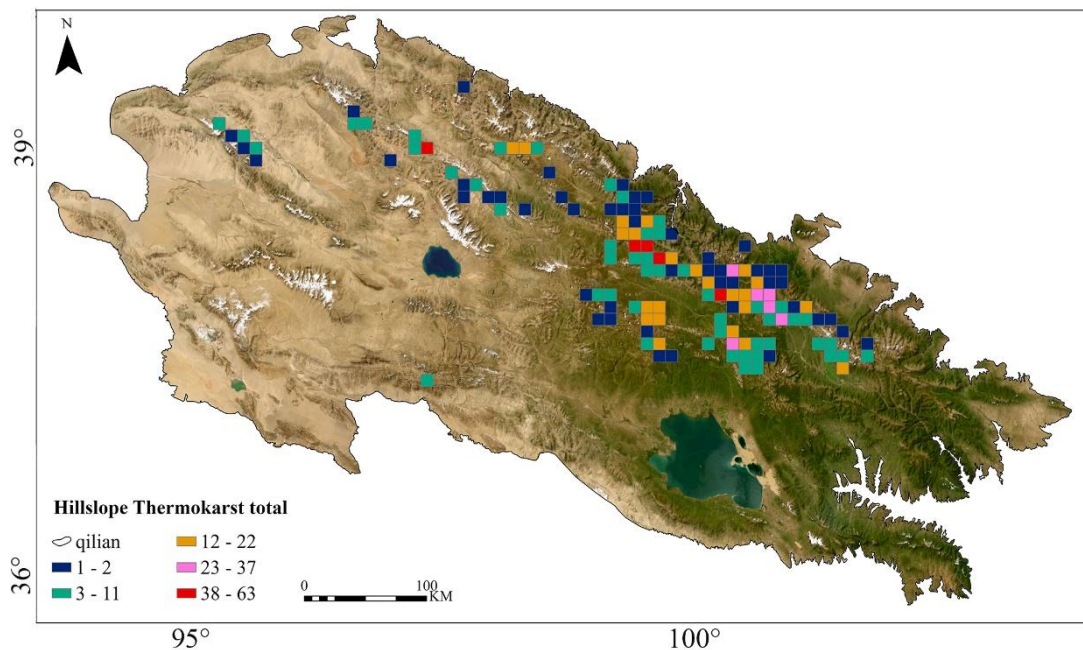
129 We collected and collated validated satellite imagery available starting in 1999 for
 130 temporal detection of the onset of the HT formation. These data include unmanned
 131 aerial vehicle imagery (e.g., Figure 1b–h) and 30 m resolution digital elevation model
 132 data from the Shuttle Radar Topography Mission (Farr et al., 2007). A combination of
 133 Omap and Google Earth software was used to detect the location of HT occurrence,
 134 and Wayback imagery provided by ESRI was used to access high-resolution (<1 m)
 135 satellite imagery and Jilin-1 satellite imagery (0.75 m) provided free of charge by
 136 China Commercial Satellite Corporation to aid in the identification (Table 1). In
 137 addition, we used digital elevation model data to calculate variables such as slope and
 138 topographic position index (TPI) of the HT. The TPI is calculated as follows (YU
 139 Hong, 2001):

$$140 \quad \text{TPI} = \log_{10} \left(\frac{E}{\text{Mean } E} + 1 \right) \times \left(\frac{S}{\text{Mean } S} + 1 \right) \quad (1)$$

141 where E is the elevation (m), S is the slope ($^{\circ}$), and Mean indicates that the mean
 142 value for the entire Qilian Mountain region is used.

143 To further analyze the distribution of HT and the analogous environmental variables,
 144 we obtain seismic data from the U.S. Geological Survey
 145 (<https://earthquake.usgs.gov/earthquakes/search/>) describing earthquakes, including

146 their timing, epicenter location, and magnitude. To categorize vegetation types into
 147 deciduous-coniferous forests (DCF), undergrowth (U), alpine scrub meadow (ASM),
 148 alpine meadow (AM), alpine grassland (AG), alpine vegetation (AV), and
 149 non-vegetated area (NA), based on data from the Resource and Environment Science
 150 and Data Center (<https://www.resdc.cn/data.aspx?DATAID=122>). To assess the
 151 relationship of air temperature and precipitation with HT, we download monthly mean
 152 air temperature and precipitation at 2 m above ground level from the fifth generation
 153 of the European Centre for Medium-Range Weather Forecasts (ECMWF) reanalysis
 154 (ERA5;
 155 <https://cds.climate.copernicus.eu/cdsapp#!/dataset/reanalysis-era5-land-monthly-means?tab=overview>).
 156
 157



158
 159
 160 **Figure 2** Frequency distribution of HT on the Qilian Mountains. The concentration of
 161 HT features is shown per 100 km² grid cell.

162
 163 **4 Methods**

164 *4.1 Manual Mapping*

165 We first quantified and mapped HT via remote sensing observations. Most
 166 occurrences of HT in the permafrost region of the Qilian Mountains since 2000 were
 167 compiled by visual interpretation in Google Earth Pro and Omap. They were also
 168 aided by high resolution (<1 m) observations from Esri Wayback Imagery, which
 169 archives all published versions of world imagery (Table 1). We used a fishnet with a
 170 mesh size of 1×1 km to segment the latest satellite imagery for the entire Qilian
 171 Mountains to quantify HT mesh by mesh. RTSs are often horseshoe shaped, tongue
 172 shaped, elongated, branched, and circle chair-shaped (Lantuit and Pollard, 2008; Yin
 173 et al., 2021), characterized by a steep backwall, low-angle bottom, and a tongue of
 174 displaced saturated soil (Lantz and Kokelj, 2008; Nicu et al., 2021). These features are
 175 tonally and morphologically different from their surroundings in color satellite images
 176 during the thawing season. RTSs also produce folded textures due to soil

177 accumulation, which appear as laterally folded stripes on imagery. Active-layer
 178 detachment slides are a common shallow landslide in permafrost areas. Their
 179 morphological characteristics vary based on vegetation cover, slope, and permafrost
 180 conditions, but common features include highly disturbed slopes, lateral shear zones,
 181 and fracture zones formed after the sliding of the active layer (Lewkowicz, 2007). We
 182 detected and sketched these features based on morphological, tonal, textural, shading,
 183 and other characteristics on remote sensing images, and then digitized their
 184 morphological features into polygonal data. Although the accuracy of this type of
 185 visual interpretation is relatively high, some HT features can be missed via this
 186 manual interpretation. To reduce such errors, satellite images of the similar period
 187 from different sources were evaluated four times using the same methods to ensure
 188 accurate results. The date of the satellite image when perturbations caused by HT can
 189 be first observed was defined as the initiation year of a particular HT feature.
 190 Depending on the initiation year, HT is categorized as occurring before 2010,
 191 2010–2015, or after 2015. To observe the temporal evolution of HT features, we used
 192 the initiation year and retraced historical images covering the Qilian Mountains, a
 193 process that also helped us distinguish between HT features and one-time transient
 194 landslides.

195

196 *4.2 Field Verification*

197 Similar HT can have different morphological characteristics due to different triggers.
 198 It is thus difficult to identify the type of HT simply through imagery. In addition, after
 199 an initial trigger and HT formation, thermokarst can evolve into different types. For
 200 example, active layer detachment slides may transition into RTS due to the exposure
 201 of subsurface ice at the trailing edge and water erosion due to thawing, which can
 202 cause the RTS to further progress into mudflows. Therefore, with visual interpretation
 203 based on imagery only providing individual snapshots, it is essential to also conduct
 204 field surveys as a validation exercise. We conducted a total of three field surveys in
 205 winter 2022, and spring and summer of 2023. Field work covered the Shiyanghe basin,
 206 Heihe basin, Datonghe basin, Qinghai Lake basin, and Shulehe basin. Due to the
 207 harsh climatic conditions and accessibility issues in the Qilian Mountains, unmanned
 208 aerial vehicles were used to survey and verify hard-to-reach areas.

209

210 **Table 1** List of the data used for manual interpretation and mapping of HT features.

Software Platform	Time Span	Resolution	Data Sources
Google Earth pro	1999–2022	0.6–15 m	Quickbird, IKONOS, etc.
Omap	since 2021	<1 m	GF-2
ESRI World Imagery	since 2014	<1 m	WorldView-3, WorldView-4, etc.
Jilin-1 website	2022	0.75 m	Jilin-1
UAV images	Feb., Apr., May 2023	~15 cm	Field Surveys

211

212 *4.3 Morphological and Spatial Statistical Analysis*

213 A landscape shape index (LSI) can be quantified to characterize shape complexity by
 214 calculating the degree of deviation of a given patch from a circle or square of the

215 same area. To quantify the shape characteristics of HT features, two LSIs are
216 calculated as follows:

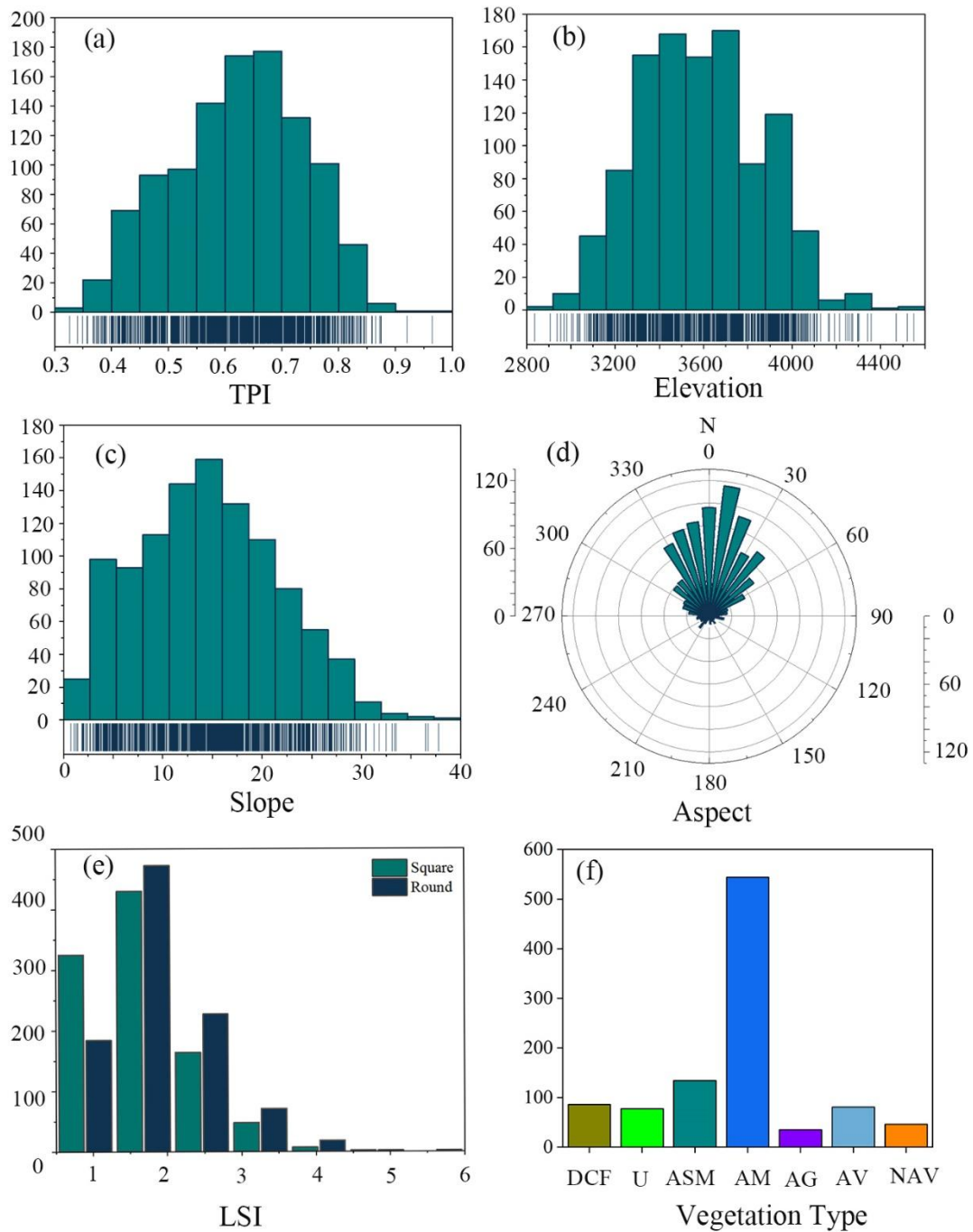
$$217 \quad LSI_{square} = \frac{0.25P}{\sqrt{A}} \quad (2)$$

$$218 \quad LSI_{round} = \frac{P}{2\sqrt{\pi A}} \quad (3)$$

219 where P is the perimeter (m) and A is the area (m²). The closer the values of LSI_{square}
220 or LSI_{round} are to 1, the more square or round the shape of the HT feature is,
221 respectively.

222 To further investigate the spatial distribution of HT, we computed a global Moran's
223 index, z-score, and p-value to determine whether there is autocorrelation in the spatial
224 distribution of HT, where p-values of z-scores are used to measure statistical
225 significance. When p-value < 0.01 and z-score > 2.58, there is a 99% probability that
226 HTs are clustered within the study area. The smaller the p-value and the larger the
227 z-score, the greater the probability that such spatial patterns are clustered. Moran's
228 index ranges from -1 to 1, with negative values corresponding to negative
229 correlations, positive values to positive correlations, and 0 denotes that the spatial
230 objects in the study area are independent of each other. Additionally, the closer the
231 index is to 1, the more clustered the HT features are, and the closer of the index is to
232 -1, the more dispersed the HT features are. To delineate the regions that may have
233 spatial autocorrelation (Bivand and Wong, 2018), we further process local
234 autocorrelation on this basis. The local autocorrelation regions are divided into four
235 types based on the local Moran's index: High-High (HH) clustering, High-Low (HL)
236 clustering, Low-High (LH) clustering, and Low-Low (LL) clustering. HH signifies a
237 region with both a higher amount of HT and neighboring regions also having a higher
238 amount of HT; HL indicates a region with a higher amount of HT surrounded by
239 neighboring regions with a lower amount of HT; LH indicates a region with a lower
240 amount of HT neighboring areas with a higher amount of HT; and LL represents a
241 region with both a lower amount of HT and neighboring regions with a lower amount
242 of HT. Although the methods described above can identify global and local spatial
243 autocorrelation, respectively, they are unable to identify clusters of concentrated HT
244 features. We therefore also apply hot spot analysis, which is another effective way of
245 exploring the characteristics of local spatial distributions. All the above techniques are
246 based on spatial statistical analysis functions in ArcGIS.

247 To explore the effects of climate on HT, we obtained the monthly mean air
248 temperature and precipitation at 2 meters above ground level from ERA5 over the
249 period 2000–2020 and calculate their annual spatial means and standard deviations
250 (Figure 6).



251
 252 **Figure 3** The number of HT terrain features (y-axes) of HT as categorized by (a)
 253 topographic position index (TPI), (b) elevation, (c) slope, (d) aspect, (e) landscape
 254 shape index (LSI), and (f) vegetation type including deciduous coniferous forests
 255 (DCF), undergrowth (U), alpine scrub meadow (ASM), alpine meadow (AM), alpine
 256 grassland (AG), alpine vegetation (AV), and non-vegetated area (NA); the blue
 257 vertical lines at the bottom of panels a–c represent the number of HT features in each
 258 x-axis bin.

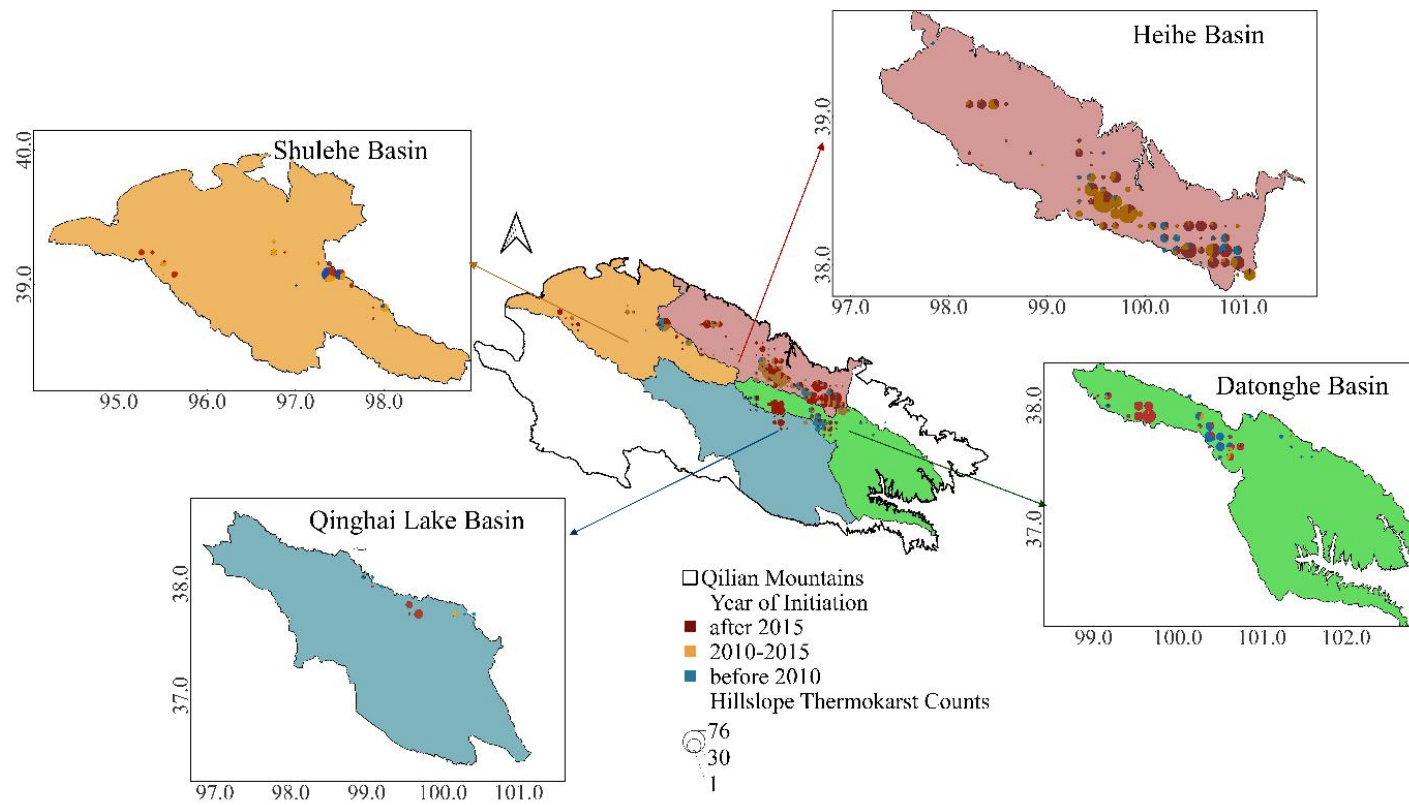
259

260 **5 Results**

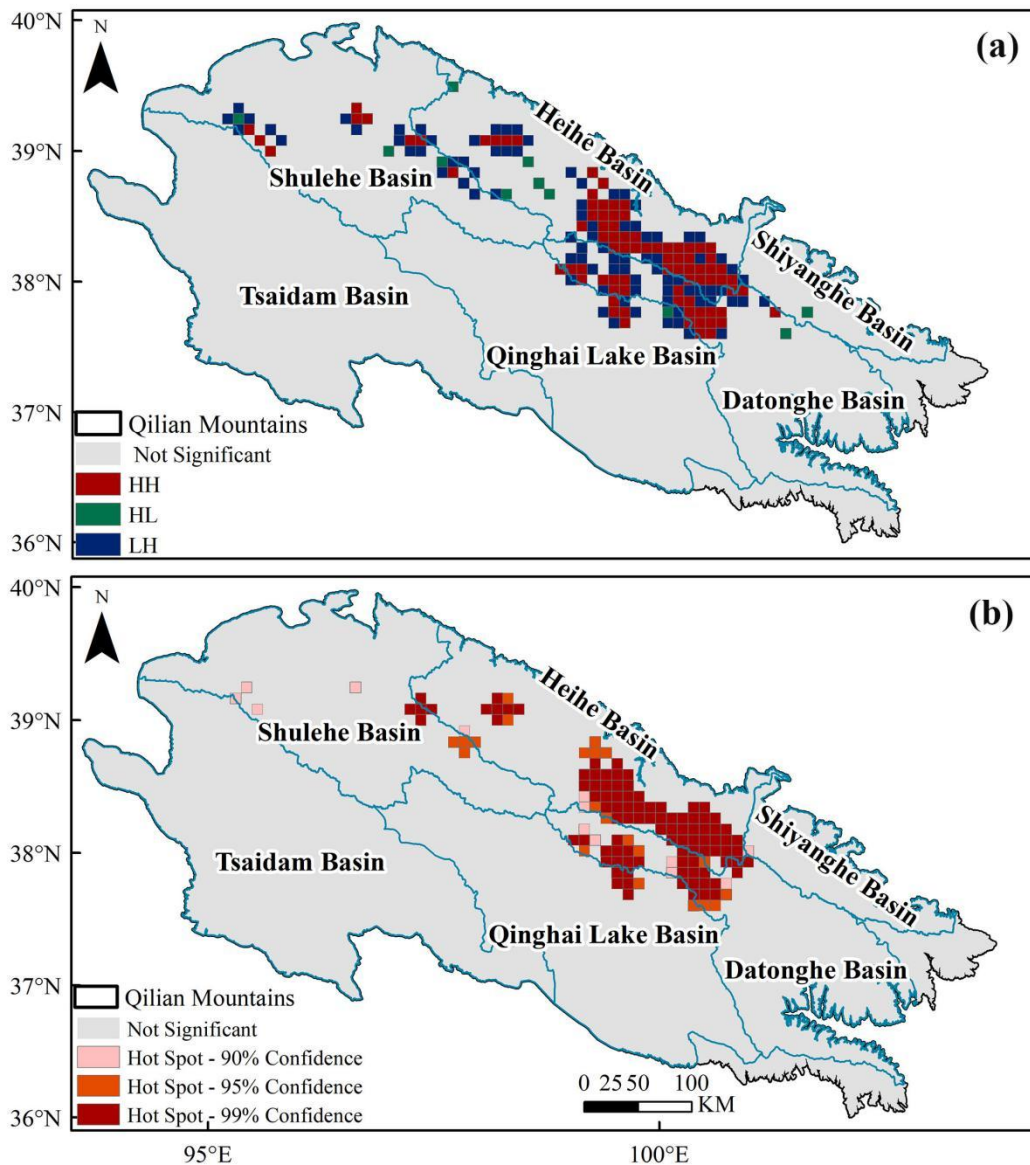
261 Our inventory of HT includes the Heihe Basin, Shulehe Basin, Datonghe Basin,
262 Shiyanghe Basin, Qinghai Lake Basin, and Tsaidam Basin within the Qilian
263 Mountains, with a total of 1064 HT features. In any 100 km² grid cell, the maximum
264 density of HT is 63 (Figure 2). This density is lower than the 68 per 25 km² in the
265 central Tibetan Plateau reported by (Luo et al., 2022) and 88 per 25 square km² on
266 Banks Island, Canada from (Lewkowicz and Way, 2019). 67% of these HT features
267 were identified in the Heihe River basin, followed by the Datonghe River Basin,
268 accounting for 19%. The HT distribution in these river basins is irregular,
269 corroborated by a positive statistically significant Moran's index value of 0.3, p-value
270 of 0.00001, and z-score of 32.5. Of all the HT features, the largest is 58 ha, the
271 smallest area is 0.01 ha, with most being smaller than 10 ha. The average area is 1.75
272 ha, with a total area of 1708 ha.

273 The spatial distribution of RTS on the QTP is strongly controlled by terrain factors
274 such as the elevation, slope, TPI, and aspect (Luo et al., 2022). The statistical results
275 indicate that HT is observed at elevations ranging from 2,835 to 4,550 m. However,
276 90% of HTs are more likely to occur at elevations ranging from 3,200 to 4,000 m in
277 the middle/high elevation area of the Qilian Mountains. HT tends to occur on
278 north-facing slopes (Figure 3b and 3d), with slopes ranging from 3° to 25° (Figure 3c).
279 In addition, the TPI shows that ~85% of the HTs occur mainly between 0.5 and 0.8
280 (Figure 3a), suggesting that they commonly occur in locations that are lower than
281 their surroundings. Both LSI indices suggest that 75% of HT has values close to 1.0
282 (Figure 3e), indicating that most HT is simple in shape and compact in morphology
283 (Niu et al., 2016). Alpine meadow areas contain ~53% of HT, followed by alpine
284 scrub meadows, which contain 13% (Figure 3f).

285 The initiation years of HT features are variable across the study area. 187 HT features
286 (18%) were identified before 2010, and the remaining 82% in the last 10 years. 392
287 sites (37%) were initiated in 2010–2015 and 482 (45%) after 2015. Much of the newly
288 initiated HT occurred in the Heihe basin and the middle and upper reaches of the
289 Datonghe basin (Figure 4), which is also a HT hotspot region. The recent increase in
290 HT can be attributed to the anomalous weather conditions in the corresponding years.
291 The association between newly observed HT and meteorological data indicates a
292 sudden HT increase in years with unusually high temperatures during the thawing
293 season (Figure 6).



294
295 **Figure 4** The timing of HT initiation within 100 km² grid cells.



296
 297 **Figure 5** (a) Spatial autocorrelation indicating high-high (HH), high-low (HL), and
 298 low-high (LH) clustering, and (b) hotspot analysis where the different colors represent
 299 the confidence levels.

300

301 **6 Discussion**

302 6.1 Drivers of HT in the Qilian Mountainous

303 6.1.1 Permafrost Conditions

304 Formation of HT is facilitated by thick subsurface ice and various internal and
 305 external environmental conditions (Stephani et al., 2023). Permafrost stability in
 306 ~80% of the permafrost area of the Qilian Mountains is predominantly transitional,
 307 and higher permafrost temperatures (Ran et al., 2021) will exacerbate the climate
 308 sensitivity of this area (Lewkowicz and Way, 2019; Patton et al., 2021) leading to
 309 melting of the subsurface ice and an increase in active layer thickness, thus decreasing
 310 the stability of the slope (Behnia and Blais-Stevens, 2018). This is also supported by
 311 our finding that ~90% of HT occurs in the transition zone between permafrost and

312 seasonally frozen soil where mean annual ground temperature is greater than -1°C .

313

314 *6.1.2 Environmental Factors*

315 Topographic conditions facilitate the formation of subsurface ice and the continuous
316 development of HT. At elevations below 5100 m on the QTP, aspect dominates the
317 distribution of permafrost. More permafrost underlies regions of shaded, north-facing
318 slopes than sunny south-facing slopes (Ran et al., 2021). Indeed, we find that $\sim 95\%$ of
319 Qilian Mountain HT is found on north-facing slopes where it also enhances vegetation
320 growth and soil moisture storage (Jin et al., 2009). Lower solar radiation, higher
321 permafrost ice content, and shallow active layer thickness (Lacelle et al., 2015; Ward
322 Jones et al., 2019) also enables HT formation (Luo et al., 2022; Niu et al., 2016; Xia
323 et al., 2022). We find more than half of the HT occurs in alpine meadows, which
324 require more water content than alpine steppes (Yin et al., 2017) and consequently
325 also results in more ground ice development under this vegetation type. We
326 determined that $\sim 90\%$ of HT in the Qilian Mountains occurs on 3° to 25° slopes. Low
327 and gentle slopes are favorable for groundwater pooling (Luo et al., 2022), whereas
328 slopes greater than 16° are relatively steep and therefore not conducive to
329 groundwater enrichment for ice formation, but such slopes also provide dynamic
330 conditions for active layer detachments and collapsing ground (Wang, 1990). We also
331 observe more HT initiation at locations that are lower compared to their surroundings,
332 as such depressions favor the accumulation of snow and rainwater (Stieglitz et al.,
333 2003) and prevent heat loss from the soil. This encourages melting of subsurface ice
334 (Zhang, 2005) at the base of the active layer and, after an unstable layer is formed
335 between the permafrost and the active layer, the overlying soil can slide along the
336 slope (Patton et al., 2021).

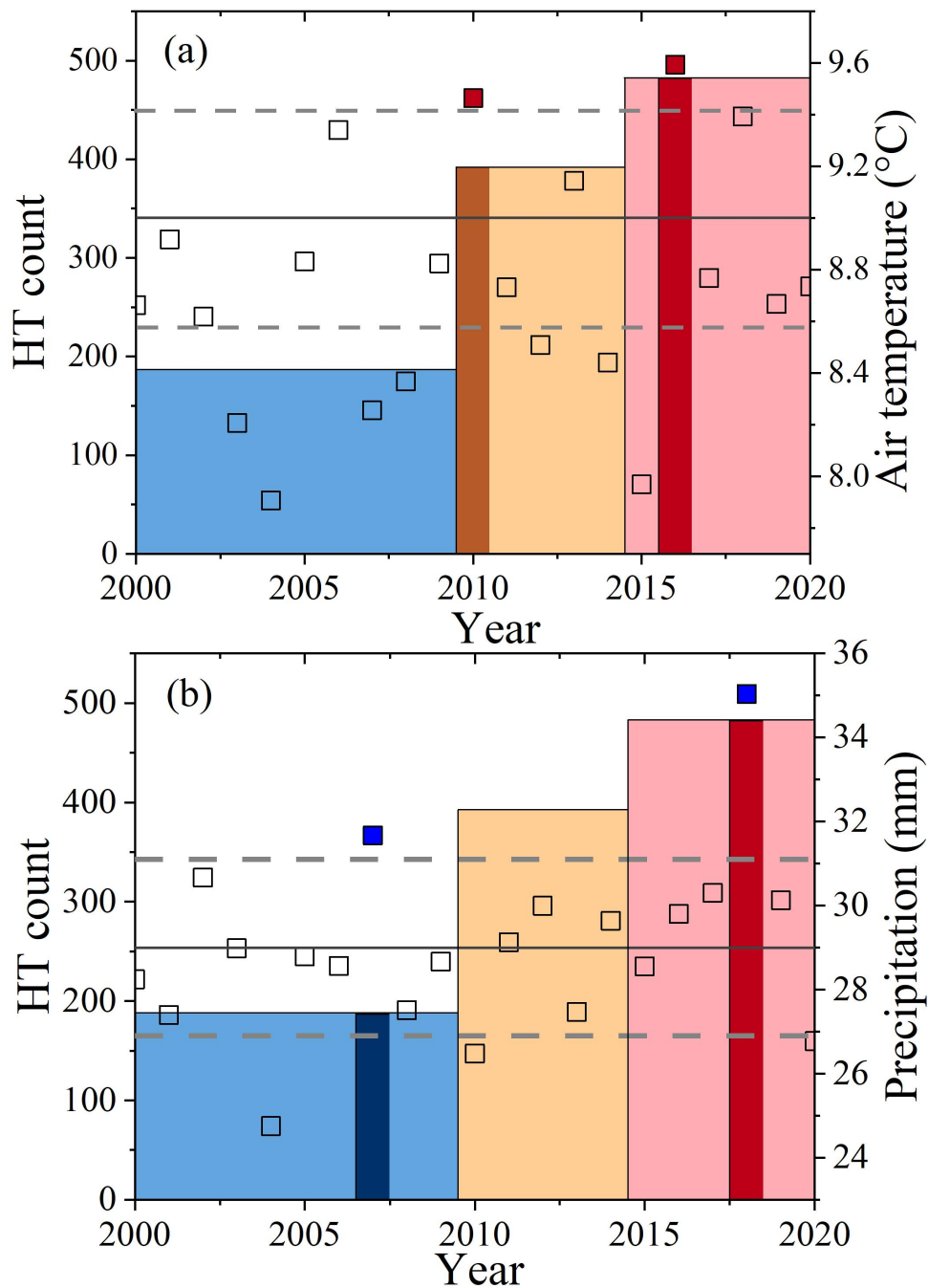
337 The Qilian Mountains were and are still formed by the ongoing collision of the Indian
338 Ocean Plate and the Eurasian Plate, resulting in the Qilian Mountains-Hexi Corridor
339 active fault system (Xiong et al., 2017) that has seen nearly 400 earthquakes of
340 magnitude 2 or greater over the past two decades. In particular, the high seismic
341 activity of the Heihe, Shiyanghe, and Datonghe Basins (Figure 7a) represents a
342 potential threat to the safety and integrity of current and future infrastructure in the
343 region. During our field investigations we found a nearly 3 km long and 2 m deep
344 slope fracture caused by a 6.9-magnitude earthquake in 2022, resulting in a massive
345 exposure of subsurface ice and the collapse of the Lanzhou-Xinjiang High Speed Rail
346 Tunnel (Figure 7b and c). The occurrence of an earthquake can result in an
347 instantaneous increase in pore water pressure and sliding forces that reduce slope
348 stability and potentially leads to a massive exposure of subsurface ice (Niu et al., 2016;
349 Xia et al., 2022), sediment liquefaction (Dadfar et al., 2017), and permafrost warming
350 due to the seismic vibrations. These vibrations lead to cracking and deformation of the
351 ice layers within the permafrost, releasing moisture and heat, consequently resulting
352 in a temperature rise of the permafrost. Additionally, earthquakes can induce the flow
353 of pore water within the permafrost, further influencing its temperature (Che et al.,
354 2014), creating the ideal setting for active-layer detachment slides. The clustering of
355 earthquake activity in the lower left corner of Figure 7a is not associated with HT
356 features, because there is no permafrost in this region.

357

358 *6.1.3 Climate Factors*

359 Extreme summer temperatures and precipitation have been identified as triggers for
360 the initiation of RTSs in many Arctic permafrost zones (Balsler et al., 2014; Kokelj et

361 al., 2015; Lewkowicz and Way, 2019; Segal et al., 2016). Given our finding that 82%
362 of HT was initiated in approximately the last decade (Figure 4), mostly during
363 2010-2015 and after 2015, we used ERA5 to determine the temperature and
364 precipitation characteristics for the Qilian Mountains over the last 20 years (Li et al.,
365 2022b) (Figure 6, the square symbols). The mean thawing season air temperatures in
366 2010 and 2016 were higher than in other years (Figure 6a, red square symbols). A
367 warming thaw season could lead to thaw consolidation at the base of the active layer
368 or to higher porewater pressure in the transient thaw layer, reducing the effective
369 shear strength, and causing slope failure (Lewkowicz and Way, 2019). The anomalous
370 air temperatures during the thawing season could accelerate permafrost thaw and
371 expose ice-rich permafrost, thus leading to new HT (Figure 6a, dark brown and dark
372 red bars, respectively). Rainfall infiltration may transfer heat to the top layer of
373 permafrost and induce melting of ground ice in ice-rich transient layers, which would
374 increase the porewater pressure at the active layer-permafrost interface and thereby
375 trigger formation of HT (Luo et al., 2022). However, precipitation variability during
376 the thawing season does not match HT formation (Figure 6b). Despite high
377 precipitation in both 2007 and 2018 (Figure 6b, blue squares), no initiation of HT was
378 found to subsequently coincide with these peaks (blue squares), and precipitation also
379 does not explain the significant initiation of HTs between 2010-2015, nor after 2015
380 (Figure 6b, yellow and red bars, respectively). The same conclusion also applies to the
381 other three sub-regions—Hoh Xil Mountain, Maqu county, and Honglianghe—and it
382 could be speculated that the nature of the soils on the QTP may instead play a role
383 (Luo et al., 2022).
384



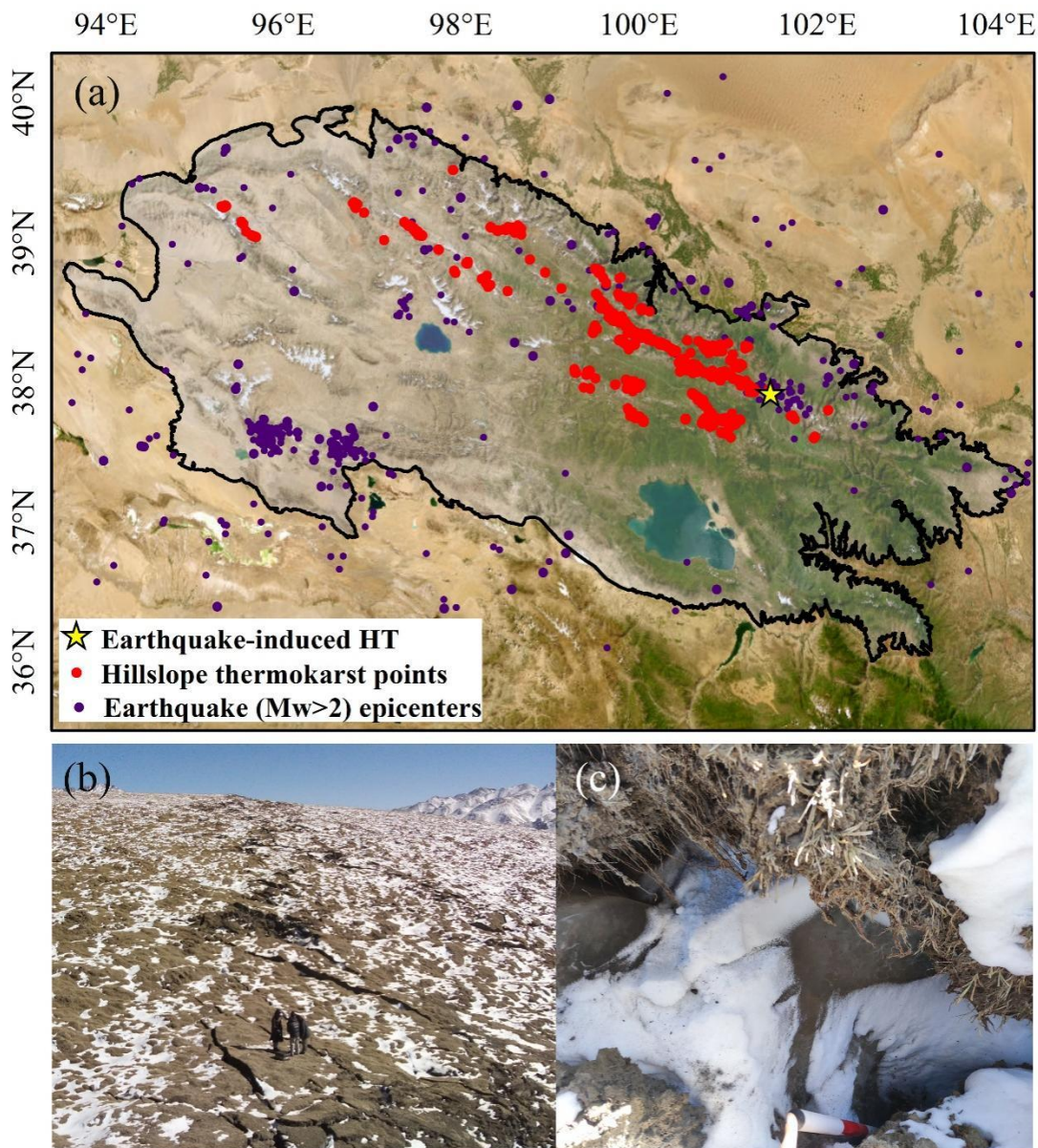
385
 386 **Figure 6** The relationship between HT numbers (variable-width bars, the darker
 387 colors represent years with extreme weather events) and (a) temperature and (b)
 388 precipitation in the thawing season from 2000 to 2020 (square symbols, the red
 389 squares and the blue squares represent the extreme weather events). The solid
 390 horizontal line represents the mean air temperature and precipitation, respectively, and
 391 the dashed lines represent ± 1 standard deviation.

392

393 6.1.4 Human Activities

394 Extensive and increasing human activities have been shown to significantly accelerate
 395 permafrost degradation (Cheng & Jin, 2013; IPCC, 2019). The total population of the
 396 Qilian Mountains is about 60,000, there are approximately 1,000 metal, energy, and
 397 other types of mineral deposits (National Mineral Properties Database 2021 Edition,

398 <http://data.ngac.org.cn/mineralresource/index.html>), and there are ~8,000 km of
 399 railroads and highways. The core of this human activity is concentrated on the eastern
 400 side of the Qilian Mountains, which generally coincides with the spatial distribution
 401 of the HT hotspots we documented. This qualitatively suggests a role of human
 402 activities on HT from, e.g., engineering disturbances, vegetation degradation due to
 403 overgrazing, etc. (Sharkhuu et al., 2007). Establishing the impact of human activities
 404 on HT quantitatively is still a difficult challenge, but our identification of the location
 405 and timing of HT formation is a first, important step for further future studies,
 406 especially on the socioeconomic development in the region.
 407



408 **Figure 7** Qilian Mountains showing (a) the location of HT locations and earthquakes
 409 with magnitude >2 in the last 20 years, (b) slope fractures caused by earthquakes, and
 410 (c) exposed subsurface ice.
 411

412

413 **7 Data Availability**

414 DEM data can be accessed through NASA

415 (<https://www.earthdata.nasa.gov/sensors/srtm>). Landsat5-8 data are available from
416 USGS (<https://www.usgs.gov/>) and Sentinel-2 from ESA (<https://www.esa.int/>), and
417 can be downloaded through Google Earth Engine. Esri World Imagery can be
418 accessed through Esri Wayback Imagery at: <https://livingatlas.arcgis.com/wayback>.
419 Some GF-2 imagery is also available online through Omap software
420 (<https://www.ovital.com/283-2/>), and high-resolution 3D satellite imagery of the
421 Qilian Mountain region can be viewed in Google Earth software. High-resolution
422 satellite images captured by the Jilin-1 satellite in China can be viewed by accessing
423 <https://www.jl1mall.com/rskit/>. The HT inventory for the Qilian Mountains can be
424 freely downloaded from the National Tibetan Plateau/Third Pole Environment Data
425 Center (<https://doi.org/10.11888/Cryos.tpcdc.300805>, Peng and Yang, 2023).

426

427 **8 Conclusion**

428 This study used visual interpretation and field investigations with repeated
429 verification to investigate HT in the permafrost zone of the Qilian Mountains. We
430 successfully produced the first HT inventory for this area, identifying a total of 1064
431 HT features. The area of these features ranged from 0.01 to 58 ha, with an average of
432 1.75 ha. Thermokarst is primarily concentrated at the junction between the upstream
433 portion of the Heihe River Basin and the mid and upstream portion of the Datonghe
434 Basin. Within a 10×10 km area, thermokarst has a maximum density of 63 features,
435 affecting an area of ~20 km². HT in the Qilian Mountains is more likely to occur on
436 north-facing shaded slopes, at elevations between 3200–4000 m, slopes of 3–25°,
437 0.5<TPI<0.8, and in alpine meadow vegetation. **Based on long-term satellite imagery,
438 874 new HT features were initiated after 2010, accounting for 82% of all HT features.
439 Of these, 392 and 482 were initiated during the periods of 2010–2015 and after 2015,
440 respectively.** Recent higher air temperatures during the thawing season are likely
441 important reasons for the intensification of HT formation in the Qilian Mountains,
442 while precipitation does not seem to play a role. **This first HT inventory for the Qilian
443 Mountains will be fundamental for quantitative assessments that explore the exact
444 causes and underlying thermokarst processes, providing observational data support for
445 automated extraction of HT features, and ultimately enhance the identification and
446 prediction of regions prone to thermokarst processes in the future. Furthermore, it will
447 facilitate the evaluation of local risk levels, potential economic losses, population
448 casualties, and other impacts, thereby furnishing governmental decision-makers and
449 relevant stakeholders with essential reference materials for mitigating potential risks.**

450

451 **Author contributions.** XP and GY designed the research and obtained funding. GY
452 analyzed the data and prepared the data files. GY, WT, XL and XP conducted the field
453 work. GY, XP, OWF, JL, CM, FN wrote the paper with input from the coauthors and
454 coordinated the analysis and contributions from all coauthors. XP and GY contributed
455 to the work equally and should be regarded as co-first authors.

456

457 **Competing interests.** The contact author has declared that neither they nor their
458 coauthors have any competing interests.

459

460 **Disclaimer.** Publisher's note: Copernicus Publications remains neutral with regard to
461 jurisdictional claims in published maps and institutional affiliations.

462

463 **Acknowledgements**

464 This work was supported by the Second Tibetan Plateau Scientific Expedition and
465 Research Program (STEP) (2019QZKK0905), the National Natural Science
466 Foundation of China (42161160328, 42171120), and the Fundamental Research
467 Funds for the Central Universities (lzujbky-2023-01).

468

469 **References**

470 Balsler, A. W., Jones, J. B., and Gens, R.: Timing of retrogressive thaw slump
471 initiation in the Noatak Basin, northwest Alaska, USA, *J. Geophys. Res. Earth Surf.*,
472 119, 1106–1120, <https://doi.org/10.1002/2013JF002889>, 2014.

473 Behnia, P. and Blais-Stevens, A.: Landslide susceptibility modelling using the
474 quantitative random forest method along the northern portion of the Yukon Alaska
475 Highway Corridor, Canada, *Nat. Hazards*, 90, 1407–1426,
476 <https://doi.org/10.1007/s11069-017-3104-z>, 2018.

477 Bivand, R. S. and Wong, D. W. S.: Comparing implementations of global and local
478 indicators of spatial association, *TEST*, 27, 716–748,
479 <https://doi.org/10.1007/s11749-018-0599-x>, 2018.

480 Che, A., Wu, Z., and Wang, P.: Stability of pile foundations base on warming effects
481 on the permafrost under earthquake motions, *Soils Found.*, 54, 639–647,
482 <https://doi.org/10.1016/j.sandf.2014.06.006>, 2014.

483 Chen, H., Zhu, Q., Peng, C., Wu, N., Wang, Y., Fang, X., Gao, Y., Zhu, D., Yang, G.,
484 Tian, J., Kang, X., Piao, S., Ouyang, H., Xiang, W., Luo, Z., Jiang, H., Song, X.,
485 Zhang, Y., Yu, G., Zhao, X., Gong, P., Yao, T., and Wu, J.: The impacts of climate
486 change and human activities on biogeochemical cycles on the Qinghai-Tibetan
487 Plateau, *Glob. Change Biol.*, 19, 2940–2955, <https://doi.org/10.1111/gcb.12277>, 2013.

488 Cheng, G. and Jin, H.: Permafrost and groundwater on the Qinghai-Tibet Plateau and
489 in northeast China, *Hydrogeol. J.*, 21, 5–23,
490 <https://doi.org/10.1007/s10040-012-0927-2>, 2013.

491 Dadfar, B., El Naggar, M. H., and Nastev, M.: Quantifying exposure of linear
492 infrastructures to earthquake-triggered transverse landslides in permafrost thawing
493 slopes, *Can. Geotech. J.*, 54, 1002–1012, <https://doi.org/10.1139/cgj-2017-0076>,
494 2017.

495 Farr, T. G., Rosen, P. A., Caro, E., Crippen, R., Duren, R., Hensley, S., Kobrick, M.,
496 Paller, M., Rodriguez, E., Roth, L., Seal, D., Shaffer, S., Shimada, J., Umland, J.,
497 Werner, M., Oskin, M., Burbank, D., and Alsdorf, D.: The Shuttle Radar Topography
498 Mission, *Rev. Geophys.*, 45, <https://doi.org/10.1029/2005RG000183>, 2007.

499 Gooseff, M. N., Balsler, A., Bowden, W. B., and Jones, J. B.: Effects of Hillslope
500 Thermokarst in Northern Alaska, *Eos Trans. Am. Geophys. Union*, 90, 29–30,
501 <https://doi.org/10.1029/2009EO040001>, 2009.

502 Huang, L., Luo, J., Lin, Z., Niu, F., and Liu, L.: Using deep learning to map
503 retrogressive thaw slumps in the Beiluhe region (Tibetan Plateau) from CubeSat
504 images, *Remote Sens. Environ.*, 237, 111534,
505 <https://doi.org/10.1016/j.rse.2019.111534>, 2020.

- 506 Huang, L., Willis, M. J., Li, G., Lantz, T. C., Schaefer, K., Wig, E., Cao, G., and
507 Tiampo, K. F.: Identifying active retrogressive thaw slumps from ArcticDEM, ISPRS
508 Journal of Photogrammetry and Remote Sensing, 205, 301–316,
509 <https://doi.org/10.1016/j.isprsjprs.2023.10.008>, 2023.
- 510 Jin, H., Li, X., Frauenfeld, O. W., Zhao, Y., Chen, C., Du, R., Du, J., and Peng, X.:
511 Comparisons of statistical downscaling methods for air temperature over the Qilian
512 Mountains, *Theor. Appl. Climatol.*, 149, 893–896,
513 <https://doi.org/10.1007/s00704-022-04081-w>, 2022.
- 514 Jin, X., Wan, L., Zhang, Y.-K., Hu, G., Schaepman, M. E., Clevers, J. G. P. W., and Su,
515 Z. B.: Quantification of spatial distribution of vegetation in the Qilian Mountain area
516 with MODIS NDVI, *Int. J. Remote Sens.*, 30, 5751–5766,
517 <https://doi.org/10.1080/01431160902736635>, 2009.
- 518 Kokelj, S. V., Tunnicliffe, J., Lacelle, D., Lantz, T. C., Chin, K. S., and Fraser, R.:
519 Increased precipitation drives mega slump development and destabilization of ice-rich
520 permafrost terrain, northwestern Canada, *Glob. Planet. Change*, 129, 56–68,
521 <https://doi.org/10.1016/j.gloplacha.2015.02.008>, 2015.
- 522 Kokelj, S. V. and Jorgenson, M. T.: Advances in Thermokarst Research: Recent
523 Advances in Research Investigating Thermokarst Processes, *Permafrost and Periglac.*
524 *Process.*, 24, 108–119, <https://doi.org/10.1002/ppp.1779>, 2013.
- 525 Lacelle, D., Brooker, A., Fraser, R. H., and Kokelj, S. V.: Distribution and growth of
526 thaw slumps in the Richardson Mountains–Peel Plateau region, northwestern Canada,
527 *Geomorphology*, 235, 40–51, <https://doi.org/10.1016/j.geomorph.2015.01.024>, 2015.
- 528 Lantuit, H. and Pollard, W. H.: Fifty years of coastal erosion and retrogressive thaw
529 slump activity on Herschel Island, southern Beaufort Sea, Yukon Territory, Canada,
530 *Geomorphology*, 95, 84–102, <https://doi.org/10.1016/j.geomorph.2006.07.040>, 2008.
- 531 Lantz, T. C. and Kokelj, S. V.: Increasing rates of retrogressive thaw slump activity in
532 the Mackenzie Delta region, N.W.T., Canada, *Geophys. Res. Lett.*, 35, L06502,
533 <https://doi.org/10.1029/2007GL032433>, 2008.
- 534 Lewkowicz, A. G.: Dynamics of active-layer detachment failures, Fosheim Peninsula,
535 Ellesmere Island, Nunavut, Canada, *Permafr. Periglac. Process.*, 18, 89–103,
536 <https://doi.org/10.1002/ppp.578>, 2007.
- 537 Lewkowicz, A. G. and Way, R. G.: Extremes of summer climate trigger thousands of
538 thermokarst landslides in a High Arctic environment, *Nat. Commun.*, 10, 1329,
539 <https://doi.org/10.1038/s41467-019-09314-7>, 2019.
- 540 Li, Y., Qin, X., Liu, Y., Jin, Z., Liu, J., Wang, L., and Chen, J.: Evaluation of
541 Long-Term and High-Resolution Gridded Precipitation and Temperature Products in
542 the Qilian Mountains, Qinghai–Tibet Plateau, *Front. Environ. Sci.*, 10, 906821,
543 <https://doi.org/10.3389/fenvs.2022.906821>, 2022.
- 544 Luo, J., Niu, F., Lin, Z., Liu, M., and Yin, G.: Thermokarst lake changes between
545 1969 and 2010 in the Beilu River Basin, Qinghai–Tibet Plateau, China, *Sci. Bull.*, 60,
546 556–564, <https://doi.org/10.1007/s11434-015-0730-2>, 2015.

- 547 Luo, J., Niu, F., Lin, Z., Liu, M., and Yin, G.: Recent acceleration of thaw slumping in
548 permafrost terrain of Qinghai-Tibet Plateau: An example from the Beiluhe Region,
549 *Geomorphology*, 341, 79–85, <https://doi.org/10.1016/j.geomorph.2019.05.020>, 2019.
- 550 Luo, J., Niu, F., Lin, Z., Liu, M., Yin, G., and Gao, Z.: Inventory and Frequency of
551 Retrogressive Thaw Slumps in Permafrost Region of the Qinghai–Tibet Plateau,
552 *Geophys. Res. Lett.*, 49, <https://doi.org/10.1029/2022GL099829>, 2022.
- 553 Mu, C., Shang, J., Zhang, T., Fan, C., Wang, S., Peng, X., Zhong, W., Zhang, F., Mu,
554 M., and Jia, L.: Acceleration of thaw slump during 1997–2017 in the Qilian
555 Mountains of the northern Qinghai-Tibetan plateau, *Landslides*, 17, 1051–1062,
556 <https://doi.org/10.1007/s10346-020-01344-3>, 2020.
- 557 Muster, S., Roth, K., Langer, M., Lange, S., Cresto Aleina, F., Bartsch, A.,
558 Morgenstern, A., Grosse, G., Jones, B., Sannel, A. B. K., Sjöberg, Y., Günther, F.,
559 Andresen, C., Veremeeva, A., Lindgren, P. R., Bouchard, F., Lara, M. J., Fortier, D.,
560 Charbonneau, S., Virtanen, T. A., Hugelius, G., Palmtag, J., Siewert, M. B., Riley, W.
561 J., Koven, C. D., and Boike, J.: PeRL: a circum-Arctic Permafrost Region Pond and
562 Lake database, *Earth Syst. Sci. Data*, 9, 317–348,
563 <https://doi.org/10.5194/essd-9-317-2017>, 2017.
- 564 Nitze, I., Grosse, G., Jones, B. M., Romanovsky, V. E., and Boike, J.: Remote sensing
565 quantifies widespread abundance of permafrost region disturbances across the Arctic
566 and Subarctic, *Nat. Commun.*, 9, 5423, <https://doi.org/10.1038/s41467-018-07663-3>,
567 2018.
- 568 Niu, F., Luo, J., Lin, Z., Liu, M., and Yin, G.: Morphological Characteristics of
569 Thermokarst Lakes along the Qinghai-Tibet Engineering Corridor, *Arct. Antarct. Alp.
570 Res.*, 46, 963–974, <https://doi.org/10.1657/1938-4246-46.4.963>, 2014.
- 571 Niu, F., Luo, J., Lin, Z., Fang, J., and Liu, M.: Thaw-induced slope failures and
572 stability analyses in permafrost regions of the Qinghai-Tibet Plateau, China,
573 *Landslides*, 13, 55–65, <https://doi.org/10.1007/s10346-014-0545-2>, 2016.
- 574 Nicu, I. C., Lombardo, L., and Rubensdotter, L.: Preliminary assessment of thaw
575 slump hazard to Arctic cultural heritage in Nordenskiöld Land, Svalbard, *Landslides*,
576 18, 2935–2947, <https://doi.org/10.1007/s10346-021-01684-8>, 2021.
- 577 Nicu, I. C., Elia, L., Rubensdotter, L., Tanyaş, H., and Lombardo, L.: Multi-hazard
578 susceptibility mapping of cryospheric hazards in a high-Arctic environment: Svalbard
579 Archipelago, *Earth Syst. Sci. Data*, 15, 447–464,
580 <https://doi.org/10.5194/essd-15-447-2023>, 2023.
- 581 Olefeldt, D., Goswami, S., Grosse, G., Hayes, D., Hugelius, G., Kuhry, P., McGuire,
582 A. D., Romanovsky, V. E., Sannel, A. B. K., Schuur, E. A. G., and Turetsky, M. R.:
583 Circumpolar distribution and carbon storage of thermokarst landscapes, *Nat.
584 Commun.*, 7, 13043, <https://doi.org/10.1038/ncomms13043>, 2016.
- 585 Patton, A. I., Rathburn, S. L., Capps, D. M., McGrath, D., and Brown, R. A.: Ongoing
586 Landslide Deformation in Thawing Permafrost, *Geophys. Res. Lett.*, 48,
587 <https://doi.org/10.1029/2021GL092959>, 2021.

- 588 Peng, X. and Yang, G.: The hillslope thermokarst inventory for the permafrost region
589 of the Qilian Mountains (2000-2020). National Tibetan Plateau Data Center[data set],
590 <https://doi.org/10.11888/Cryos.tpdc.300805>, 2023.
- 591 Ran, Y., Li, X., Cheng, G., Nan, Z., Che, J., Sheng, Y., Wu, Q., Jin, H., Luo, D., Tang,
592 Z., and Wu, X.: Mapping the permafrost stability on the Tibetan Plateau for
593 2005–2015, *Sci. China Earth Sci.*, 64, 62–79,
594 <https://doi.org/10.1007/s11430-020-9685-3>, 2021.
- 595 Segal, R. A., Lantz, T. C., and Kokelj, S. V.: Acceleration of thaw slump activity in
596 glaciated landscapes of the Western Canadian Arctic, *Environ. Res. Lett.*, 11, 034025,
597 <https://doi.org/10.1088/1748-9326/11/3/034025>, 2016.
- 598 Sharkhuu, A., Sharkhuu, N., Etzelmüller, B., Heggem, E. S. F., Nelson, F. E.,
599 Shiklomanov, N. I., Goulden, C. E., and Brown, J.: Permafrost monitoring in the
600 Hovsgol mountain region, Mongolia, *J. Geophys. Res.*, 112, F02S06,
601 <https://doi.org/10.1029/2006JF000543>, 2007.
- 602 Stephani, E., Darrow, M. M., Kanevskiy, M., Wuttig, F., Daanen, R. P., Schwarber, J.
603 A., Doré, G., Shur, Y., Jorgenson, M. T., Croft, P., and Drage, J. S.: Hillslope erosional
604 features and permafrost dynamics along infrastructure in the Arctic Foothills, Alaska,
605 *Permafr. Periglac. Process.*, 34, 208–228, <https://doi.org/10.1002/ppp.2188>, 2023.
- 606 Stieglitz, M., Déry, S. J., Romanovsky, V. E., and Osterkamp, T. E.: The role of snow
607 cover in the warming of arctic permafrost, *Geophys. Res. Lett.*, 30,
608 <https://doi.org/10.1029/2003GL017337>, 2003.
- 609 Wang, R., Peng, Q., Zhang, W., Zhao, W., Liu, C., and Zhou, L.: Ecohydrological
610 Service Characteristics of Qilian Mountain Ecosystem in the Next 30 Years Based on
611 Scenario Simulation, *Sustainability*, 14, 1819, <https://doi.org/10.3390/su14031819>,
612 2022.
- 613 Ward Jones, M. K., Pollard, W. H., and Jones, B. M.: Rapid initialization of
614 retrogressive thaw slumps in the Canadian high Arctic and their response to climate
615 and terrain factors, *Environ. Res. Lett.*, 14, 055006,
616 <https://doi.org/10.1088/1748-9326/ab12fd>, 2019.
- 617 Xia, Z., Huang, L., Fan, C., Jia, S., Lin, Z., Liu, L., Luo, J., Niu, F., and Zhang, T.:
618 Retrogressive thaw slumps along the Qinghai–Tibet Engineering Corridor: a
619 comprehensive inventory and their distribution characteristics, *Earth Syst. Sci. Data*,
620 14, 3875–3887, <https://doi.org/10.5194/essd-14-3875-2022>, 2022.
- 621 Xiong, J., Li, Y., Zhong, Y., Lu, H., Lei, J., Xin, W., Wang, L., Hu, X., and Zhang, P.:
622 Latest Pleistocene to Holocene Thrusting Recorded by a Flight of Strath Terraces in
623 the Eastern Qilian Shan, NE Tibetan Plateau, *TECTONICS*, 36, 2973–2986,
624 <https://doi.org/10.1002/2017TC004648>, 2017.
- 625 Yang, D., Qiu, H., Ye, B., Liu, Y., Zhang, J., and Zhu, Y.: Distribution and Recurrence
626 of Warming-Induced Retrogressive Thaw Slumps on the Central Qinghai-Tibet
627 Plateau, *J. Geophys. Res. Earth Surf.*, 128, e2022JF007047,
628 <https://doi.org/10.1029/2022JF007047>, 2023.

- 629 Yin, G., Niu, F., Lin, Z., Luo, J., and Liu, M.: Effects of local factors and climate on
630 permafrost conditions and distribution in Beiluhe basin, Qinghai-Tibet Plateau, China,
631 *Sci. Total Environ.*, 581–582, 472–485,
632 <https://doi.org/10.1016/j.scitotenv.2016.12.155>, 2017.
- 633 Yin, G., Luo, J., Niu, F., Lin, Z., and Liu, M.: Machine learning-based thermokarst
634 landslide susceptibility modeling across the permafrost region on the Qinghai-Tibet
635 Plateau, *Landslides*, 18, 2639–2649, <https://doi.org/10.1007/s10346-021-01669-7>,
636 2021.
- 637 YU Hong, J. Z., ZENG Hui: Study on Distribution Characteristics of Landscape
638 Elements along the Terrain Gradient, *SCIENTIA GEOGRAPHICA SINICA*, 21, 64,
639 <https://doi.org/10.13249/j.cnki.sgs.2001.01.64>, 2001.
- 640 Zhang, T.: Influence of the seasonal snow cover on the ground thermal regime: An
641 overview, *Rev. Geophys.*, 43, <https://doi.org/10.1029/2004RG000157>, 2005.
- 642